Geophysical Journal International

Geophys. J. Int. (2026) **245,** 1–14
Advance Access publication 2026 January 28
Research Paper

https://doi.org/10.1093/gji/ggag043

Reservoir related seismicity changes around the Gotvand Dam (south west of Iran)

Behnam Maleki Asayesh,[1,2] Sebastian Hainzl,[2] Mohammad Tatar,[3] Gert Zöller[1] and Saeed SoltaniMoghadam[3]

[1]*University of Potsdam, Institute of Mathematics, Karl-Liebknecht-Str.* 24-25, 14476 *Potsdam, Germany. E-mail: maleki@gfz.de*
[2]*GFZ Helmholtz Centre for Geosciences, Telegrafenberg* 14473 *Potsdam, Germany*
[3]*International Institute of Earthquake Engineering and Seismology (IIEES), Department of Geophysics, No.*21 *Arghavan St. Tehran, Iran*

Accepted 2026 January 26. Received 2025 October 15; in original form 2025 June 4

SUMMARY

Over the past few decades, the global number of dams has increased substantially. Water impounded behind these dams, resulting in elevated crustal pore pressure and altered stress distribution around reservoirs, could potentially trigger or suppress the failure of nearby faults, leading to transient changes in seismicity. In this study, we analyse 14 yr (2006–2019) of spatiotemporal seismicity recorded by a dense local network in the Gotvand area (SW Iran), covering about 5.5 yr before and 8.5 yr after impoundment. The initial catalogue, comprising over 48 000 relocated earthquakes, was reduced to 6464 background events by adopting a 3-D Epidemic-Type Aftershocks Sequence declustering model with a cut-off magnitude of 1.3. We analyse the spatiotemporal background seismicity pattern in the Gotvand area in comparison with calculated reservoir-related spatiotemporal stress changes relative to the initial stress state before water impoundment, approximating the Gotvand reservoir by 726-point sources covering the reservoir surface. We find that following the initiation of impoundment, the local background seismic activity slightly increased during the impounding, pointing to induced/triggered seismicity. However, most importantly, the impoundment of Gotvand lake has altered the spatial seismicity patterns, leading to a notable reduction in seismic activity in the central area of the reservoir, which is in agreement with the calculated negative Coulomb stress changes in the same area. Using the Coulomb-Rate-and-State seismicity model, we find that the spatiotemporal seismicity response due to the calculated stress changes is consistent with the observations.

Key words: Earthquake interaction, forecasting, and prediction; Induced seismicity; Seismicity and tectonics; Statistical seismology.

1 INTRODUCTION

The number of earthquakes associated with anthropogenic activities (induced seismicity) has increased significantly since the beginning of the last century (G.R. Foulger *et al.* 2018) and has become of interest to both non-scientific and scientific communities. Induced seismicity can occur close to densely populated areas, and discriminating it from natural seismicity is a highly debated topic. Many outstanding cases with moderate magnitude caused by human-related activities have been reported and compiled in different studies (e.g. A. McGarr *et al.* 2002; R. Davies *et al.* 2013; W.L. Ellsworth 2013; G.R. Foulger *et al.* 2018). Induced earthquakes are caused by human operations such as water impoundment, mining, geothermal power production, hydrocarbon extraction, hydraulic fracturing for shale gas extraction, CO_2 sequestration, wastewater injection and cyclic injection and extraction operations at underground gas storage (T. Dahm *et al.* 2010; W.L. Ellsworth 2013; F. Grigoli *et al.* 2017; G.R. Foulger *et al.* 2018, 2022; A.P. Rinaldi *et al.* 2020; M. Jamalreyhani *et al.* 2021). Stress perturbations due to man-made operations have the potential to advance failure on active faults that are prone to natural failure in the future (T. Dahm *et al.* 2013). In this way they can also trigger large events. Furthermore, stress changes caused by human operations can nucleate small events that cascade into larger events according to the Epidemic-Type Aftershocks Sequence (ETAS) hypothesis (e.g. Y. Ogata 1998; H. Ebrahimian *et al.* 2022).

Anomalous increases in seismicity around water reservoirs have been linked to the induced stress from the water impoundment behind the dams. In particular, reservoir impoundments can drive nearby faults to failure by increasing crustal pore pressure and Coulomb stress changes (K. Deng *et al.* 2010; G.R. Foulger *et al.* 2018). Furthermore, various key aspects such as the time to maximum water level, the reservoir area itself, the height of the maximum water column, and variations in hydrogeological conditions or the crustal faulting regime have been recognized to affect the spatiotemporal seismicity patterns near reservoirs (e.g. H.K. Gupta *et al.* 1972a, b; H.K. Gupta 2002; X. Qiu & C. Fenton 2015; G.R. Foulger *et al.* 2022).

The earliest report of reservoir-triggered seismicity (RTS) was from Lake Mead, Nevada and Arizona, USA (D.S. Carder 1945). Since that time many probable reservoir-induced earthquakes have been reported, some of which have resulted in fatalities and extensive property damage. Xinfengjiang Reservoir (China), Koyna Dam (India), Nurek Dam (Tadjikistan) and Aswan Dam (Egypt) are some of the notable examples with the most known RTS ($M > 6$) that have been well studied (H.K. Gupta *et al.* 1972b; W. Leith *et al.* 1981; D.W. Simpson & S.K. Negmatullaev 1981; C. Keith *et al.* 1982; M. Awad & M. Mizoue 1995; P. Talwani 1995; H.K. Gupta 2002; X. Lei 2011). By now (June 2025) more than 230 reported cases of RTS listed in HIQuake database (https://inducedearthquakes.org) (M. Wilson *et al.* 2017). The 2008 M_w7.9 Wenchuan, China, earthquake with tens of thousands fatalities, is the largest earthquake claimed to have been induced with the water impoundment of the Zipingpu dam (e.g. X. Lei *et al.* 2008; S. Ge *et al.* 2009; R.A. Kerr & R. Stone 2009; X. Lei 2011). However, other researchers believe that the Wenchuan earthquake was a natural event from aspects of either phenomenological or mechanical analysis (Y. Chen 2009) and the small Coulomb stress changes induced in the rupture zone by the filling of the dam (K. Deng *et al.* 2010). The reservoir-triggered seismicity of the Atatürk Dam, the fifth largest dam on Earth, has recently been studied by P. Büyükakpınar *et al.* (2021), who showed that two moderate earthquakes, M_w5.5 in 2017 and M_w5.1 in 2018, occurred near the reservoir where the induced stress was focused. While they found that the reservoir impoundment led to the locking of the faults beneath the reservoir, the overall effective stress in the seismogenic zone increased over decades due to pore-pressure diffusion. This interplay can explain the enhanced background seismicity in the reservoir area, which is anticorrelated with the water-level.

In Iran, reservoir-triggered seismicity has not been comprehensively studied so far, although reservoirs have been impounded in seismically active regions. In particular, a number of dams have been built on the Karun River, which rises in the Zard Kuh in the Zagros Mountains of western Iran, flows south and west, and continues to the Persian Gulf. This river is 950 km long and is the wateriest, largest and longest river in Iran. The dams have been built mainly for hydroelectric power generation, agricultural purposes, and flood control. Karun-1 (Shahid Abbaspour Dam), Karun-3, Karun-4, Masjed Soleyman Dam, and Gotvand Dam are all on the main stem. Gotvand Dam, located in the downstream of Masjed Soleyman Dam, with a total height of 180 m and a total water capacity of 4.5 billion m^3 is the highest rock-fill dam with a central clay core and the second largest reservoir in Iran. This dam is located in the Zagros Simply Folded Belt (SFB), one of the main tectonostratigraphic domains of the Zagros Mountains. The Zagros range in southwestern Iran is known as one of the most seismically active regions, having experienced both historical and instrumental large earthquakes (Fig. 1).

The seismicity of the Gotvand region has been continuously monitored by a dense local seismological network since 2006 (about five and half years before the impoundment of the Gotvand Dam). Additionally, detailed topographical data of the underwater area of the reservoir have been meticulously compiled through precise mapping procedures before impoundment. The precise catalogue of about 14 yr (2006–2019) from the local network, the underwater topographical information and the daily time history of water levels enable us to study the relationship between reservoir impoundment and seismicity in detail. For that purpose, we first remove aftershocks, which can distort the signatures of RTS, using the recently developed 3-D ETAS model (B.M. Asayesh *et al.* 2023a, 2025). We then investigate the statistical characteristics of the seismicity of the Gotvand area in three time periods, including pre-impounding (before impoundment), impounding (from impoundment until the first peak of water level) and post-impounding (after the first peak). We also calculate the Gutenberg–Richter *b*-value for these periods and investigate correlations between water level and seismicity. Finally, we calculate the spatiotemporal stress at seismogenic depths induced by the reservoir due to loading and pore pressure diffusion and apply the Coulomb-Rate-and-State seismicity model (J. Dieterich 1994; E.R. Heimisson & P. Segall 2018). We show that the spatiotemporal patterns of the stress calculations and resultant seismicity changes are consistent with the observations in the Gotvand region.

2 GOTVAND DAM, SEISMICITY AND SEISMOLOGICAL SETTING

2.1 Seismotectonic setting

The Karun River and its built-up dams are situated in the Zagros active belt, the most active seismotectonic zone of the Iranian plateau. The Zagros orogenic belt is the result of the opening and closure of the Neo-Tethys oceanic realm. The belt is considered to be a complex product of an early Mesozoic separation of the Iranian continental block from the rest of the Gondwana landmasses following by a NE-dipping subduction of the newly generated Neo-Tethyan oceanic crust below the Iranian microcontinent and subsequent collision between the Arabian and Iranian plates (M. Alavi 1980; M. Berberian & G. King 1981; A.C. Şengör 1984). The Zagros mountain belt is approximately 1500 km long, 250–400 km wide and extends from eastern Turkey, where it connects to the North- and East-Anatolian faults, to the Oman Gulf, where it dies out at the Makran subduction zone. The NW–SE striking Zagros Mountains, as a central part of the Alpine-Himalayan orogenic belt, accommodate approximately one-third of the current Arabian–Eurasian convergence ($\sim$2–3 cm yr^{-1}) (e.g. P. Vernant *et al.* 2004; F. Khorrami *et al.* 2019).

The Mesopotamia-Persian Gulf Foreland Basin, the Zagros Fold-Thrust Belt (ZFTB), and the High Zagros Zone are the three primary tectonostratigraphic domains from SW to NE that make up the Zagros Mountains. Gotvand Dam are located in the SFB, which with Zagros Foredeep Zone and the Mountains Front Flexure Zone are three subdomains of the ZFTB (M. Berberian 1995; A. Bahroudi & H. Koyi 2003; A. Bahroudi & H.A. Koyi 2004; M. Alavi 2007). The SFB is the lower-elevation part of

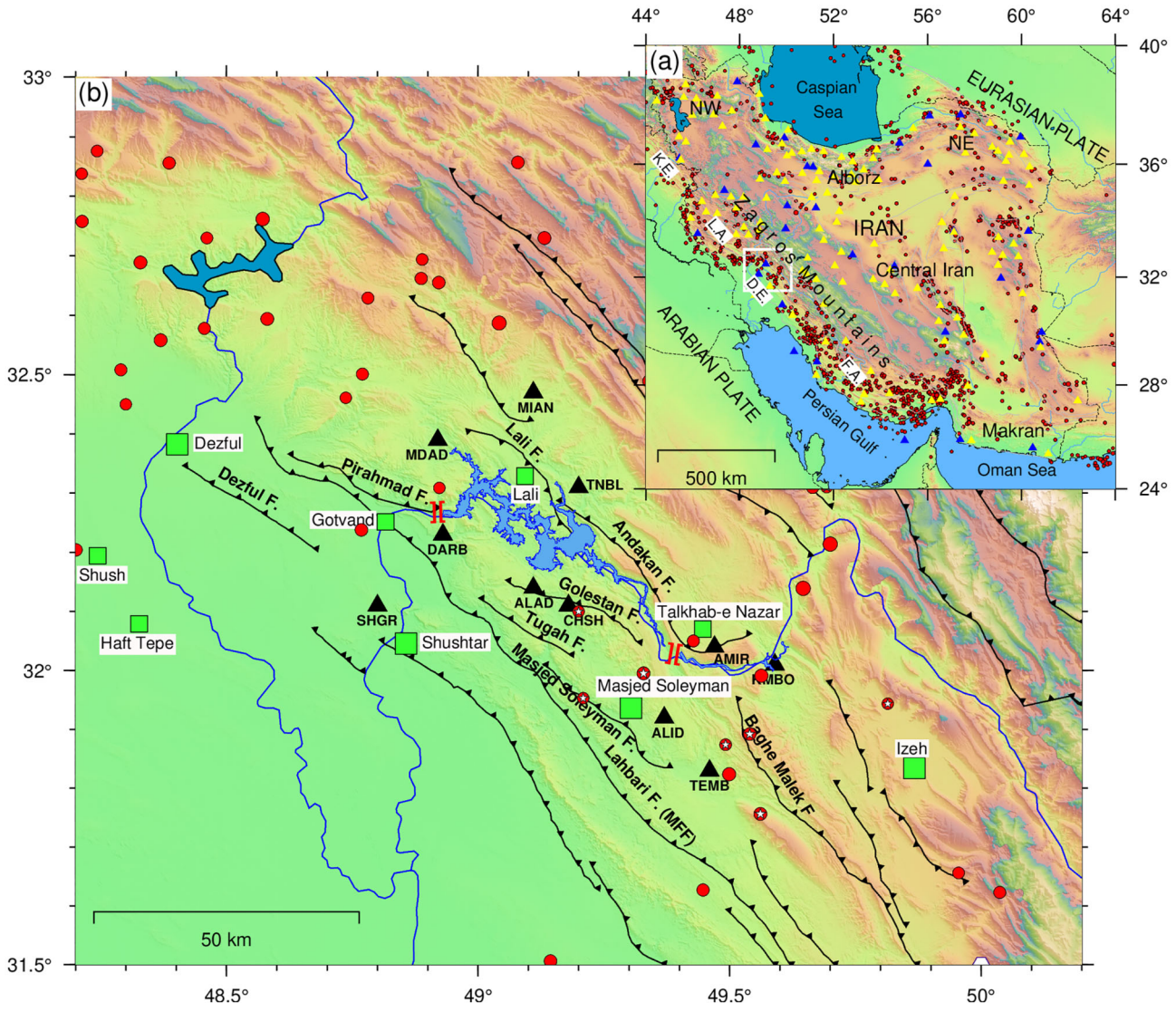

Figure 1. (a) The Iranian plateau and its seismotectonic settings. The Kirkuk Embayment (K.E.), Lurestan Arc (L.A.), Dezful Embayment (D.E.) and Fars Arc (F.A.) from NW to SE are four tectonostratigraphic domains of the most active part of the Zagros (the Simply Folded Belt). Grey lines depict the main active faults of this plateau and the Gotvand area is outlined by the white rectangle. Yellow and blue triangles indicate the IRSC and IIEES stations, respectively. (b) Zoom on the Gotvand area. Black lines show major mapped active faults. Large green squares indicate major cities, the small green squares depict small towns, and the black triangles indicate the location of seismic stations of the Gotvand local seismological networks. Red circles in both panels are $M > 5.0$ earthquakes during 1900– 2022 from the USGS catalogue. Red circles with white stars inside them in panel (b) are $M > 5.0$ earthquakes since 2002 in the area from the USGS catalogue.

the range where most of the active deformation in the Zagros is concentrated and is subdivided laterally into four physiographic provinces from NW to SE, namely the Kirkuk Embayment, the Lurestan Arc, the Dezful Embayment and the Fars Arc (Fig. 1) (e.g. J. Stoecklin 1968; K. Hessami *et al.* 2001; M. Alavi 2007; B. Oveisi *et al.* 2009).

The master blind thrust faults, such as the Main Zagros Thrust Fault, Mountain Front Fault known also as the Lahbari Fault, the Main Recent Fault, the High Zagros Fault and the Zagros Foredeep Fault, are the most dominant faults in Zagros. These faults which mainly separate Zagros to domains and subdomains follow its NW–SE trend and abruptly shifts southward at the eastern syntaxis of the Fars Arc to link up with structures in the Makran accretionary wedge (e.g. M. Berberian 1995; V. Regard *et al.* 2004; F. Yamini-Fard *et al.* 2007; A. Edey *et al.* 2020). Zagros is famous for its abundant earthquakes with low to moderate magnitude (W.D. Barnhart *et al.* 2013). The larger earthquakes, distributed across an ∼200 km wide zone, commonly occur on blind faults (M. Berberian 1995) with focal depths ranging from 8 to 14 km (e.g. J. Ni & M. Barazangi 1986; C. Baker *et al.* 1993; K. Hessami *et al.* 2001; B.M. Asayesh *et al.* 2018, 2023b; M. Metz *et al.* 2023).

The reservoir of the Gotvand Dam is located in the north part of the Dezful Embayment and surrounded with active faults such as Dezful, Pirahmad, Lali, Andakan, Golestan, Tugah, Masjed Solayman, Lahbari and Baghe Malek faults, which dominate the regional tectonics in the study area (Fig. 1). A detailed study of the historical earthquakes occurred before 1900 in the Gotvand region (N.N. Ambraseys & C.P. Melville 2005) indicates the absence of any important historical seismicity within an

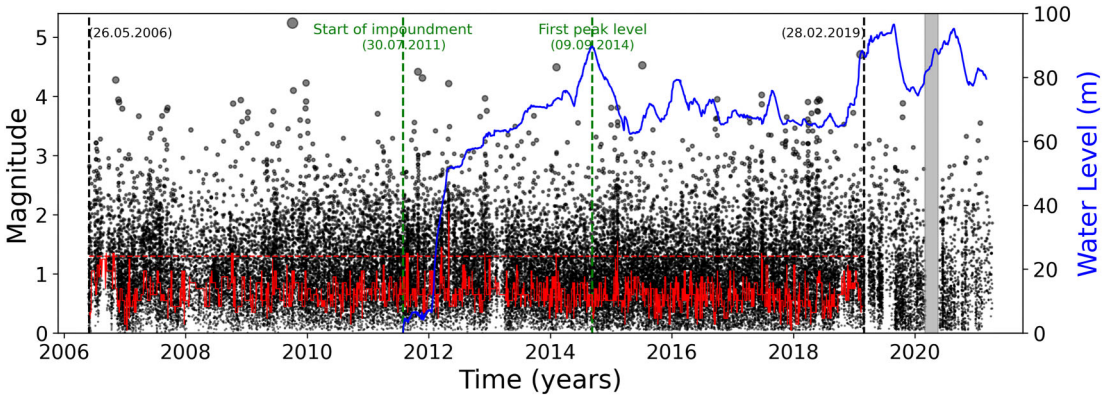

Figure 2. Magnitudes as a function of the times of events recorded by the local network ($M > 0$). The two vertical dashed black lines depict the start and end times (before the 2019 heavy flood) of the data set used in the analysis. The thick grey column shows the time of data gap due to the coronavirus pandemic. The blue curve (with the scale on the right) refers to the water level of the Gotvand Dam. The left dashed green line shows the impoundment time (2011.07.30) of the Gotvand Dam, and the right one shows the first peak of its water level (2014.09.09). The temporal variation of the magnitude of completeness (MaxC) is shown in red, while the horizontal dashed red line indicates the selected cut-off magnitude of 1.3.

Table 1. The characteristics of the Gotvand Dam and reservoir.

Characteristics	Gotvand Dam
Dam type	rock-fill
Construction time	1998–2011
Filling of water	July, 2011
Dam height (m)	234
Dam length (km)	90
Reservoir capacity (m^3)	4.5 billion
Surface area (km^2)	96.5
Min. water level (m)	133.70
Max. water level (m)	230.25

Table 2. 1-D velocity structure of the Gotvand and Masjed Soleyman region used for earthquake localization (M. Tatar 2010).

V_p (km s^{-1})	Depth (km)
4.70	0.0
5.25	4.0
5.95	10.0
6.35	14.0

area with a radius of 50 km from the dam site (Fig. 1). Important events such as the 840 Ahvaz, 1052 Baghe-Malek ($M \sim 6.8$) and 1666 Zagros ($M \sim 6.5$) earthquakes were located quite far from the study region. Regarding the large events, there are several events with magnitudes even greater than 5 (red circles in Fig. 1b). Since 2002, about 10 earthquakes ($M \geq 5.0$) have occurred in the area mainly located southeast of the Gotvand lake (red circles with white stars inside in Fig. 1b and Table S1, Supplementary Material).

2.2 Gotvand Dam

The upper Gotvand Dam (Gotvand-e Olya), or simply the Gotvand Dam, is constructed on the Karun River in Khuzestan province, Iran. This clay-cored rock-filled dam is the highest dam in Iran and its reservoir, with an area of ∼96.5 km^2 (total volume of 4.5 billion m^3) at height of 234 m above sea level, is the second largest after the Karkhe reservoir (M. Ebrahimi *et al.* 2018). The construction of the Gotvand Dam took about 18 yr from 1998 to 2011 and the impoundment of the reservoir started on 2011 July 30 (left green vertical line in Fig. 2). From the beginning of impoundment until 2012 January 20, the water level increased only slightly (from 133.7 m until 140.3 m). After that the rate of water level increment increased and has reached one of its peaks with 223.42 m on the September of 2014 (right green vertical line in Fig. 2). The highest water level was recorded on August 2019 due to previous heavy spring flood (Fig. 2 and Table 1).

2.3 Seismic network and seismicity distribution

We used an approximately 14-yr seismic catalogue of the Gotvand–Masjed Soleyman local seismological network (Fig. 1 and Table S2, Supporting Information). This seismic network consists of 10 stations belonging to the Gotvand project of the Iran Water and Power Resource Development Co. (IWPCO) and to the Masjed Solyman Dam of the Khuzestan Water and Power Authority (KWPA), and one station (Shushtar–SHGR) from the Iranian National Broad-band Seismological Network (BIN) of the International Institute of Earthquake Engineering and Seismology (IIEES). It was designed and installed by IIEES and has been in operation since 2006 (Fig. 1b). The local seismic network consists of very high quality Taurus recorders and Trillium 40 (40 s–50 Hz) seismometers manufactured by Nanometrics Company. Each seismic station operates at a sampling rate of 80 Hz. To control the timing of the recorded seismograms, a GPS was connected to the recorder, which synchronized it by sending hourly timing pulses. Furthermore, to reduce the azimuthal gap and improve location accuracy, we incorporated data from two permanent seismological networks in Iran: (1) the Iranian Seismological Center (IRSC) network, which operates more than 120 three-component broad-band and short-period stations and (2) the BIN of IIEES, comprising 35 three-component broad-band stations (Fig. 1a).

The data were analysed in the manner described by M. Tatar *et al.* (2004, 2005, 2011). All earthquakes were relocated using an appropriate local velocity model (Table 2) obtained from simultaneous inversion for a 1-D velocity structure and hypocentres (E. Kissling 1988) using well-located local earthquakes recorded by the Gotvand and Masjed Soleyman seismic networks (M. Tatar 2010).

From 2006 May 26 to 2021 April 10, 48 436 events with magnitudes ranging from −0.9 to 5.2 were recorded by this local network. Fig. S1 (Supplementary Material) shows the epicentral and depth distribution of all recorded data. We remove all explosions/blasts (due to oil and gas exploration and dam construction) from the catalogue, knowing their approximate location and time of occurrence (47 414 events remained). Focal depths of well-located earthquakes show that the majority of reliable seismic events were located at depths between 7 and 17 km, mostly within the crystalline basement. Fig. 2 shows the magnitudes as a function of the time of these recorded earthquakes. In March 2019, a heavy flood occurred in the area, causing an interruption in the seismic network and data gathering. Furthermore, at the beginning of the coronavirus pandemic in 2020, there is a gap of about 81 d (2020.03.04–2020.05.24) in our catalogue (thick grey column in Fig. 2) due to difficulties in visiting the stations and gathering the recorded data. Because of the pandemic situation, the problem of checking the stations and gathering the data continued for several months. Therefore, events after February 2019 are not included in our analysis. The two vertical dashed black lines in Fig. 2 represent the duration of the data set we use in our analysis. Furthermore, some of the well-recorded data are located far from the local dam network. Therefore, we only consider the events inside a polygon surrounding the dam region (Fig. S1, Supporting Information).

2.4 Focal mechanism

The dense seismological network in the epicentral area of the earthquakes reduces the difficulties of assigning take-off angles to regional phases (e.g. refracted waves) and provides better coverage of the focal sphere than possible with teleseismic or regional recordings. However, the quality of the focal mechanism solution depends strongly on the number of stations. We analyse focal mechanisms of earthquakes recorded by the local network using the first arrival polarities of *P*-waves. This approach involved projecting the rays emanating from the earthquake source across different take-off angles toward seismic stations positioned at various azimuths relative to the event's epicentre on the surface.

Using at least seven *P*-wave polarities on the focal sphere, we determined focal mechanisms for 23 events that occurred before impoundment (Table S3, Supporting Information) and 16 events after impoundment (Table S4, Supporting Information). These analyses were conducted to identify the predominant tectonic regime of the area and to select the appropriate receiver fault parameters for the subsequent stress calculations. Taking into account the number and quality of the polarity measurements, the type of waves (direct or refracted) and the azimuthal distribution on the focal sphere, we categorize the focal mechanisms into two groups. Category A includes mechanisms where all three quadrants are sampled and for which both nodal planes are constrained within 20°. Category B comprises mechanisms where only one nodal plane is well defined, but the orientations of the P and T axes are determined within 20°. The fault plane between the two nodal planes can only be identified by analysing the spatial distribution, particularly in this study, through the geometry of the seismicity with depth. The best quality mechanisms (category A) are presented in red, and those belonging to category B are shown in green in Fig. 3. Source mechanism solution maps for 16 earthquakes that occurred after impoundment, illustrating the primary polarity distribution of the seismic stations, are presented in Fig. S2 of the Supplementary Material. We also consider 11 Global Centroid Moment Tensor (gCMT) focal mechanisms (M_w 4.8–6.1, see Table S5 in Supplementary Material), which occurred since 1977 in the study area (black beach balls in Fig. 3).

Apart from a few strike-slip mechanisms, the majority of the focal mechanisms solutions indicate reverse faulting, known to be the dominant mechanism in Zagros (Fig. 1). Although the seismicity distribution is rather defused, several alignments related to the surface traces of known active regional faults can be recognized. Computed focal mechanisms mainly indicate NW-trending reverse faults dipping toward either NE or SW. According to the distribution of earthquakes on cross-sections, the dip was towards the northeast (M. Tatar 2010). The strikes of these earthquakes concentrate in NW–SE direction 120° and 300°. However, NE-dipping of some focal mechanisms, consistent with gentle dip alignment of seismicity, indicates the existence of NW-trending NE-dipping low-angle reverse faults. Based on observed alignments across the NE-trending sections, the geometry of active faults is divided mainly into three categories: gentle dip of 25° towards NE related to the Lahbari fault, high-angle dip of 60° towards NE, related to active faults like Pirahmad, Tougah, Golestan, Masjed Soleyman and Andakan and high-angle dip of 65° towards SW related to activity of the Lali fault.

3 STATISTICAL ANALYSIS OF THE EARTHQUAKE CATALOGUE

3.1 Completeness and frequency–magnitude distribution

For our selected catalogue (events between 2006.05.26 and 2019.28.02 and inside the polygon), we estimated the magnitude of completeness (M_c) by two different standard procedures, namely the fast and straightforward Maximum Curvature (MaxC) and the Entire Magnitude Range (EMR) methods (Y. Ogata & K. Katsura 1993; M. Wyss *et al.* 1999; S. Wiemer & M. Wyss 2000). The MaxC method defines M_c by the maximum of the magnitudes' histogram, which is equivalent to the maximum value of the first derivative of the cumulative frequency–magnitude distribution. It is known to often underestimate M_c. In contrast, the EMR method considers an error function as detection probability in combination with the Gutenberg–Richter distribution to fit the entire distribution. The first approach yields a completeness magnitude of 0.65, and the application of the latter approach yields $M_c = 1.2$ using a 90 per cent detection probability threshold for the smallest events (Fig. 4a). To be on the safe side, we use 1.3 as the cut-off magnitude and consider events with a magnitude equal to or greater than 1.3 in our analysis. We also performed a time-dependent analysis of M_c using the MaxC method to assess its variation over the study period. The results indicate that M_c remained below 1.3 for most of the period, with only brief increases attributable to episodes of elevated seismicity (Fig. 2). Altogether, we have 9541 $M \geq 1.3$ events inside our selected polygon that occurred from 2006 May 30, until 2019 February 28. Fig. 5 illustrates the epicentral and depth distribution of this data set.

We investigate our catalogue using the well-established Gutenberg–Richter (GR) relation for the frequency–magnitude

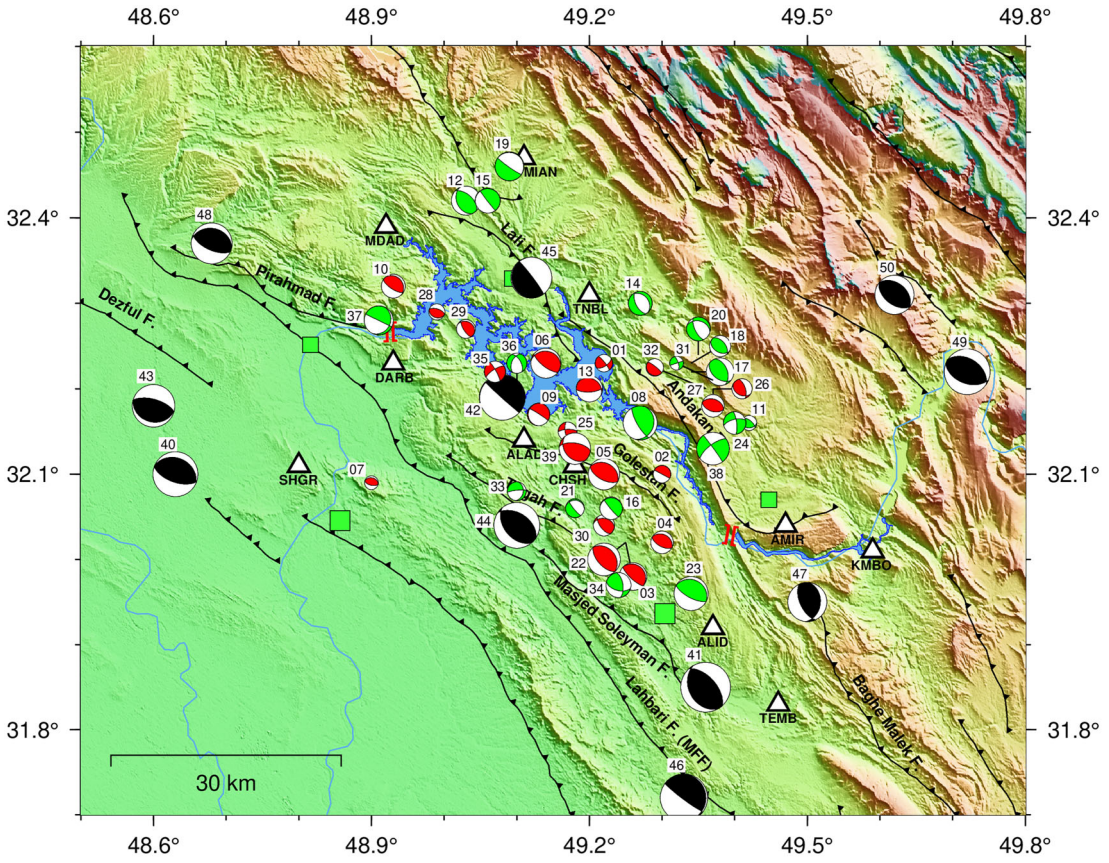

Figure 3. Map of the focal mechanisms (equal-area lower hemisphere) of events in the Gotvand area, derived by recordings of the local network. The earthquake mechanisms are divided into two categories based on their quality. The best-quality mechanisms belonging to category A are presented in red, and those belonging to category B are shown in green. Black beach balls depict focal mechanisms of earthquakes from gCMT with magnitudes (M_w 4.8–6.1) during 1977–2021.

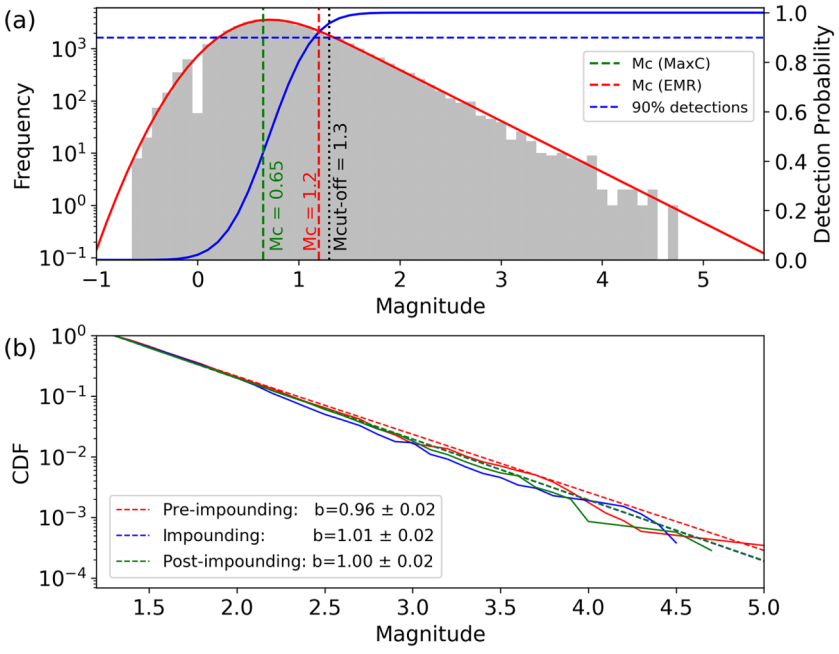

Figure 4. (a) Non-cumulative frequency–magnitude distribution, where the completeness magnitude (M_c) is estimated as 0.65 according to the maximum curvature (MaxC) method, while the fit of the Y. Ogata & K. Katsura (1993) model (solid lines) yields 1.2 for detection probabilities of 90 per cent for the lowest magnitude (dashed horizontal line). (b) Cumulative distribution function (solid lines) for pre-impounding (red), impounding (blue) and post-impounding (green) periods, with maximum likelihood estimations of the corresponding *b*-values (dashed lines) in the legend.

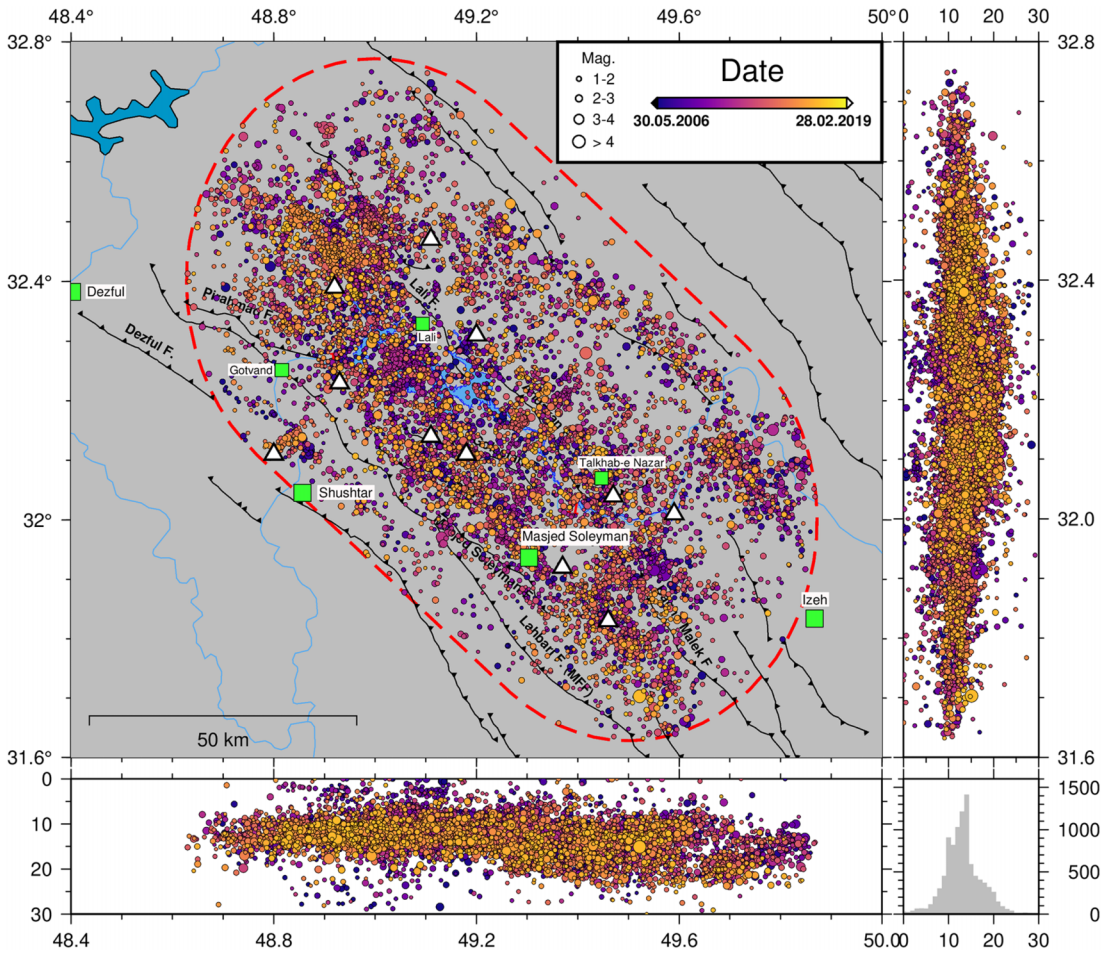

Figure 5. Epicentral and depth distribution of the $M \geq 1.3$ earthquakes recorded by the local network from 2006 May 30, until 2019 February 28, inside the selected polygon around the Gotvand Dam. The colour of the circles depicts the time. The black solid lines in the map show the main active faults, and the white triangles are the local network stations. The histogram in the bottom right depicts the depth distribution of selected events.

distribution. This relation states that the number of events (N) with magnitudes above a value M follows the simple relation $\log(N) = a - bM$. Here, the a-value represents the total seismicity rate, which can largely vary between different tectonic regions, and the b-value determines the relation between the frequency of small and large earthquakes and is usually found to scatter around 1.

The frequency–magnitude distributions of the earthquakes together with GR-fits for our selected catalogue (2006.05.26–2019.02.28) and three successive periods including before impoundment, pre-impounding, (2006.05.26–2011.07.30), after impoundment until the first peak of water level, impounding, (2011.07.31–2014.09.09) and after the first peak of water level, post-impounding, (2014.09.10–2019.02.28) are shown in Fig. 4(b). The b-value of GR distribution is estimated as 0.99 ± 0.01, 0.96 ± 0.2, 1.01 ± 0.02 and 1.00 ± 0.02 for the whole data and the three successive periods, respectively. The b-value for the pre-impounding period is less than 1.0, but it increases a little during the impounding and post-impounding periods.

3.2 Declustering

Earthquake catalogues are essentially a mix of two populations: dependent and independent events. Independent earthquakes or so-called background events are caused by tectonic loading or aseismic stress transients such as reservoir-induced stress changes. They are not related to earthquake–earthquake interactions and, thus, not triggered by previous earthquakes. The second population of earthquakes in a catalogue are aftershocks that are thought to be dependent, triggered by mechanical processes at least partly controlled by previous earthquakes. Aftershocks should be removed from the catalogue to reveal the potential changes in the spatial and temporal seismicity patterns with the reservoir impoundment.

We use the recently developed 3-D ETAS model (B.M. Asayesh *et al.* 2023a, 2025) to separate aftershocks and background events in our data set. In this model, the earthquake rate R at the hypocentral location $\vec{x}$ and time t is the sum of the background rate μ and the ongoing aftershock activity of past events, where the latter are given by their occurrence times, hypocentres, and magnitudes $t_i, \vec{x}_i, M_i$. It is described by:

$$R(\vec{x}, t) = \mu(\vec{x}) + \sum_{i:t_i<t} K\, 10^{\alpha(M_i - M_c)}\, (c + t - t_i)^{-p}\, f(|\vec{x} - \vec{x}_i|, m_i). \quad (1)$$

In this model, the total number of aftershocks increases exponentially by the magnitude of the triggering event with the scaling parameter α, and the temporal decay of aftershocks is

Table 3. Estimated 3-D ETAS parameters for $M \geq 1.3$ events between 2006.05.30 and 2019.02.28.

Model	μ [1/d]	K	α	c [d]	p	d_0	γ	q	A	$\tilde{\mu}$	$\tilde{\sigma}$	AIC
ETAS[a]	1.44	0.015	0.39	0.012	1.40	0.84	0.07	1.59	–	–	–	142 683
ETAS[b]	1.44	0.005	0.37	0.012	1.40	0.78	0.08	1.46	36.05	14.59	0.3	142 475

[a]ETAS model with uniform K-value.
[b]ETAS model with depth-dependent K-value.

described by the Omori–Utsu law (T. Utsu *et al.* 1995) in terms of the parameters c and p. The spatial trigger function f given by an isotropic power law of the distance $r = |\vec{x} - \vec{x}_i|$ according to

$$f(r, M_i) = c_n \left[\left(d_0 10^{\gamma M_i} \right)^2 + r^2 \right]^{-(1+q)} . \quad (2)$$

We follow the approach described in detail in B.M. Asayesh *et al.* (2023a). Due to the absence of moderate to large events, we treated earthquakes as point sources and employed an isotropic spatial kernel in our ETAS model. In particular, we estimate the ETAS parameters together with a 3-D varying background rate by the maximum likelihood method using two different approaches. In the initial approach, we assume a constant trigger potential (K-value). In the second approach, we consider that K varies with depth z according to $K(z) = K \cdot [1 + A \cdot h(z, \tilde{\mu}, \tilde{\sigma}) \cdot H(z)]$, where H is the Heaviside function and h the lognormal distribution with parameters $\tilde{\mu}$ and $\tilde{\sigma}$. Table 3 provides the estimated results using the $M \geq M_c = 1.3$ events between 2006.05.30 and 2019.02.28 inside the selected polygon. To compare the fits, that is, the maximum loglikelihood values ($\mathcal{L}L_{max}$), of both model variants having a different number of parameters (N_p), we use the Akaike Information Criterion (AIC) given by AIC $= 2(N_p - \mathcal{L}L_{max})$. AIC estimates each model's quality relative to others, with the best model indicated by the lowest AIC. The results show that the 3-D ETAS model with depth-dependent K-value fits significantly better the Gotvand data set, in accordance with the results for California presented by B.M. Asayesh *et al.* (2023a).

In the following, we identify the background events using the parameters estimated by the maximum likelihood method for the model with depth-dependent K-value (Table 3). For this purpose, we determine the probability for each event to belong to the background activity by the ratio between the background rate and the total earthquake rate at the events' occurrence time and location (for more information see B.M. Asayesh *et al.* 2023a). Using a probability threshold of 0.5, we separate our data set to 6464 background and 3077 aftershocks. Figs S3 and S4 (Supplementary Material) depict epicentre and depth distributions of the background events and aftershocks separately. For a consistency check, we compare our declustering results from the 3-D ETAS approach with the results of the independent, well-established nearest-neighbour distances method (M. Baiesi & M. Paczuski 2004, 2005; I. Zaliapin *et al.* 2008; I. Zaliapin & Y. Ben-Zion 2013). The results for both methods are similar, demonstrating the consistency of our approach (Fig. S5, Supplementary Material).

3.3 Temporal variations of seismicity and water levels

Fig. 6 shows the magnitude versus time distribution of the background (blue circles) and triggered (grey circles) events and the monthly total seismicity (grey) and background (blue) rates. Here, the background rate is calculated by summing the probability of each earthquake being a background event, using the ETAS model with its estimated parameters. In particular, the background probability of an event with index i is given by the ratio $\mu(\vec{x}_i)/R(\vec{x}_i, t_i)$. In case of a truly constant background rate, the result should fluctuate around the mean value with a Poissonian variability. In contrast, real temporal variations of the background rate would be reflected in larger variations, while ETAS parameters might be slightly biased due to an incorrect model assumption.

Based on the cumulative number of background events (Fig. 6a), following the initiation of impoundment, the average background seismicity rate experiences only minor changes during and after the impounding period, justifying the use of the ETAS model with a constant background rate in time. During the pre-impounding period, the average seismicity rate equals 1.29, which increases to 1.54 events per day in the impounding period and then decreases to 1.39 events per day in the last period, when the water level varied less. However, those changes are almost insignificant, considering that the background rate was already evaluated the last two years before the impoundment, with an average rate of 1.45 events per day.

We also compare the temporal evolution of earthquake activity after impoundment with the water level variations. We find no significant correlation or anticorrelation between the earthquake rate and water level changes (Fig. 6b). We calculated the Pearson's correlation coefficient for earthquake rates and water levels calculated in bins of 30 d. The highest correlation coefficient $r_p = 0.27$ with a p-value of 0.05 is observed for the post-impounding period. However, Spearman's rank correlation indicates no correlation ($r_s = 0.23$, $p = 0.10$) for the same period. Furthermore, the results for the correlation between water levels and delayed seismicity by 1 to 3 months show no improvement.

3.4 Spatial distribution

We separately investigate the spatial distribution of pre and post-background seismicity before and after the start of the impoundment, respectively. For that purpose, we smoothed the background events in the corresponding time interval and divided the resulting values by the duration of the period. Here, we used adaptive smoothing, where each event is smoothed with a Gaussian distribution with a standard deviation equal to the distance to its 10th nearest neighbour but considering a minimum value of 5 km. Figs 7(a) and (b) illustrate the spatial density rate of background seismicity in the pre and post-period. The seismicity rate change, that is, the difference between the seismicity rates in both periods, is shown in Fig. 7(c). It shows that upon the commencement of impoundment, a considerable seismicity decrease occurred in the central area of the reservoir, while some moderate activation occurred in the surroundings. Some studies have reported that seismicity occurring in close proximity to reservoir shores (typically within about 20 km) is more strongly

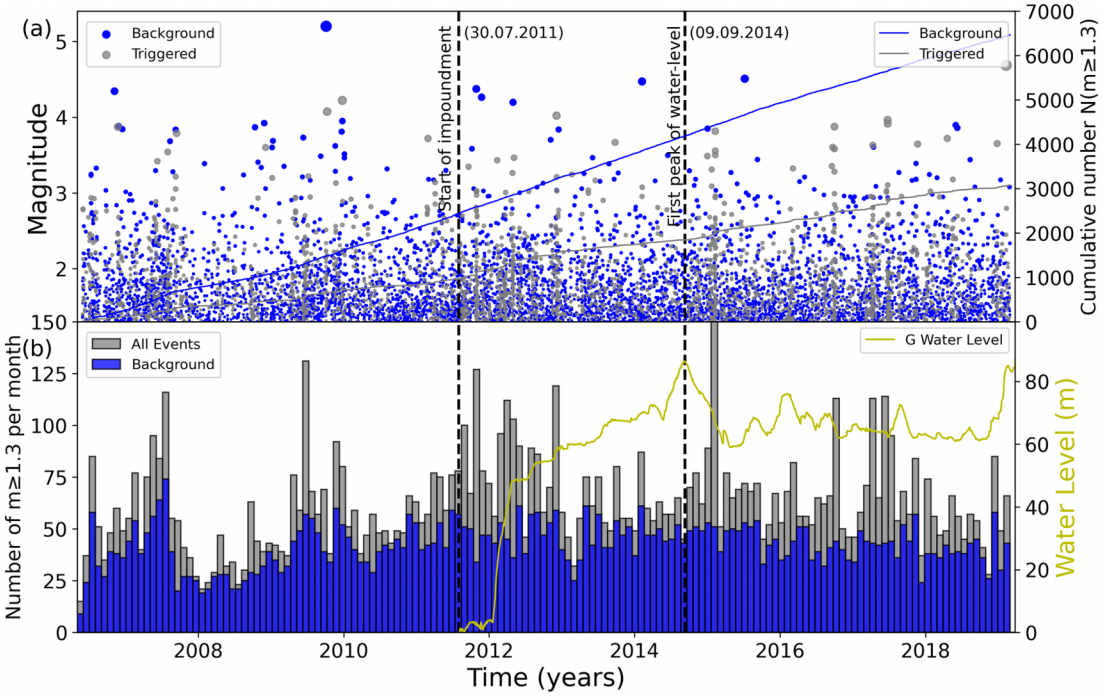

Figure 6. (a) Magnitude–time distribution of the background (blue circles) and triggered (grey circles) events with the scale on the left and cumulative number of background (blue line) and triggered (grey line) with the scale on the right. (b) The time evolution of the water level with values referring to the changes relative to the start of the impoundment and the earthquake activity ($M \geq 1.3$).

correlated with water level changes than more distant events (e.g. M. Imoto 2001; K. Pavlou 2019). To account for this, we reanalysed our data set by restricting it to earthquakes within 20 km of the reservoir shore. The results, however, remained fully consistent with those obtained from the complete data set (Fig. S6, Supporting Information).

4 MODELLED RESERVOIR-INDUCED STRESSES AND SEISMICITY CHANGES

We calculate the reservoir-related stress changes relative to the initial stress state before water impoundment using a semi-analytical approach, which has been widely adopted in similar studies of reservoir-triggered seismicity (e.g. K. Gahalaut & A. Hassoup 2012; S. Hainzl *et al.* 2014; P. Büyükakpınar *et al.* 2021). This method was selected due to the limited availability of detailed subsurface structural and mechanical data necessary for constructing a robust finite element model. The semi-analytical approach provides a practical and efficient way of quantifying stress perturbations while ensuring the transparency and reproducibility of the modelling assumptions. To achieve this, we assume a uniform and isotropic half-space and represent the Gotvand reservoir by 726-point sources covering the reservoir surface (see Fig. S7 in Supplementary Material). Utilizing the available accurate topographical map of the region beneath the Gotvand lake, alongside the daily historical records of water levels, we have acquired the water column height h for each specific point source (x_i, y_i) as function of time t, that is, $h(x_i, y_i, t)(i = 1, \ldots, 726)$.

The total stress changes related to a reservoir are due to two main mechanisms, namely (1) the elastic stress changes resulting from the surface load of the water, and (2) the change in pore pressure diffusion due to the water intrusion into depth, ΔP_d (E.A. Roeloffs 1988). We calculated those stress changes on a three-dimension grid with spacing of 0.02°. For each grid point, we calculate both contributions by summing the solutions for all 726 point sources representing the Gotvand reservoir.

The stress change tensor $\Delta\sigma_{ij,c}$ related to the instant undrained loading effect is calculated by means of the 3-D Boussinesq–Cerruti solution for a point force acting on the surface of an infinite half-space (see e.g. K. Deng *et al.* 2010), and the instant pore-pressure change due to the loading effect is determined by $\Delta P_\mathrm{c} = -B(\Delta\sigma_{11,\mathrm{c}} + \Delta\sigma_{22,\mathrm{c}} + \Delta\sigma_{33,\mathrm{c}})/3$, where B is the Skempton coefficient. The delayed pore pressure changes ΔP_d due to diffusion into depth z is calculated by the convolution of the observed reservoir water height h with the Green's function G (K. Gahalaut & A. Hassoup 2012; S. Hainzl *et al.* 2014)

$$\begin{aligned}
&\Delta P_\mathrm{d}(x, y, z, t) \\
&\quad = D \sum_{i=1}^{726} A_i \int_{-\infty}^{t} \rho\, g\, h(x_i, y_i, \bar{t}) \\
&\times G(x - x_i, y - y_i, z, t - \bar{t})\, d\bar{t} \\
&\text{with } G(x - x_i, y - y_i, z, t - \bar{t}) \\
&\quad = \frac{z}{8\pi^{1.5}[D(t - \bar{t})]^{2.5}}\, e^{-\frac{(x-x_i)^2+(y-y_i)^2+z^2}{4D(t-\bar{t})}}
\end{aligned} \tag{3}$$

where parameters g, ρ and D refer to the gravitational constant, the water density and the hydraulic diffusivity, respectively. A_i is the reservoir area related to the point-source indexed by i. The total time-dependent stress change tensor $\Delta\sigma_{ij}$ consisting of both contributions is calculated by $\Delta\sigma_{ij} = \Delta\sigma_{ij,c} - \delta_{ij}\Delta P_\mathrm{d}/B$ with δ_{ij} being the Kronecker delta function.

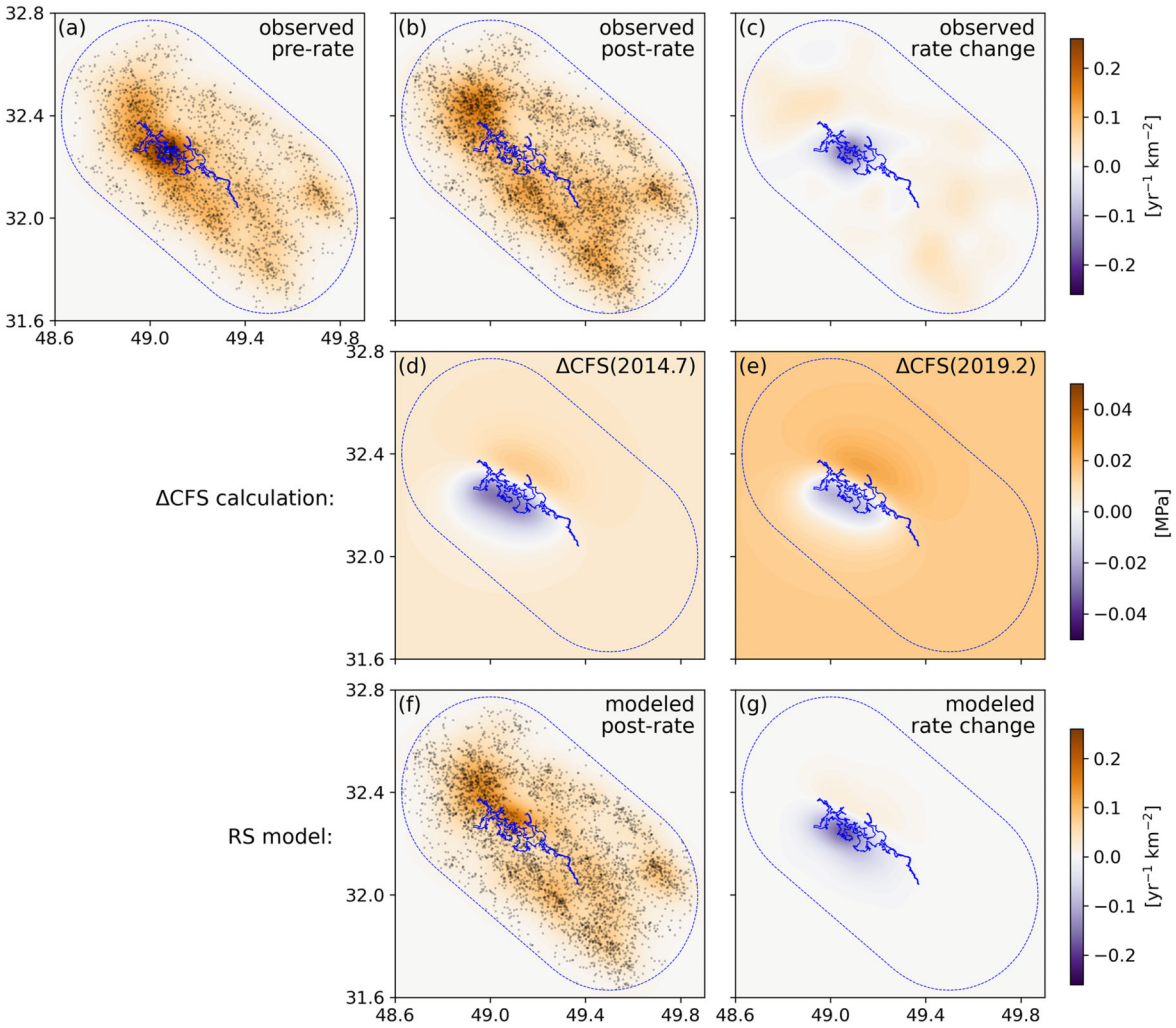

Figure 7. Map of seismicity rates and stress changes: Observed colour-coded seismicity rates in the (a) pre and (b) post-impoundment periods result from smoothing the observed background events that occurred in those periods (grey points). (c) The corresponding rate change of the observed background activity. (d, e) Calculated ΔCFS at the first peak of the water level in September 2014 and at the end of our calculation time (February 2019), where stress is calculated at 12.5 km depth for a receiver mechanism with strike = 300°, dip = 60°, and rake = 85°, considering a tectonic stressing rate of 2 kPa yr^{-1}. Panels (f) and (g) depict in correspondence to (b, c) the seismicity rate and rate changes calculated using the RS model based on the determined spatiotemporal stress evolution. In all panels, the blue dashed line shows the selected buffer area and the blue solid line indicates the Gotvand lake outline.

We calculate the time-dependent Coulomb Failure Stress (CFS) changes for the dominant focal mechanism of the Gotvand area as the receiver mechanism. For the given slip direction, first the change of the shear stress $\Delta\tau$ and the compressional normal stress $\Delta\sigma_n$ is calculated based on $\Delta\sigma_{ij}$. Then ΔCFS is determined by $\Delta\text{CFS} = \Delta\tau - \mu(\Delta\sigma_n - \Delta P)$ with friction coefficient μ and pore pressure change $\Delta P = \Delta P_c + \Delta P_d$. In our calculation, we use the dominant mechanisms in the Gotvand area as receiver mechanisms. Specifically, we define a strike of 300°, a dip of 25° and 60°, and a rake of 85°, while setting $B = 0.5$, $\mu = 0.8$ and Poisson ratio equal to 0.3. Hydraulic diffusivity (D) in the crust can vary across several orders of magnitude. It is often hypothesized to be higher along faults due to their increased permeability and interconnected fracture networks, which enhance both porosity and fluid transport compared to the surrounding intact rock, resulting in higher effective hydraulic diffusivity (S.A. Shapiro *et al.* 1997). By analysing the evolution of reservoir-induced seismicity, P. Talwani & S. Acree (1984) reported hydraulic diffusivity values ranging from 0.5 to 50 m^2 s^{-1}, while C.H. Scholz (1990) suggested a narrower range of 1–10 m^2 s^{-1} based on a a synthesis of seismicity-based studies. S.A. Shapiro *et al.* (1997) later developed a method to estimate permeability from seismic emissions induced by borehole fluid injections, yielding an upper crustal diffusivity on the order of 1 m^2 s^{-1}. In this study, we adopt $D = 1.0$ m^2 s^{-1} and assume it to be spatially uniform over all the domain.

The calculated stress changes are less than 50 kPa at seismogenic depth. Therefore, tectonic loading has to be considered in our analysis. For that purpose, we use the linear relation of B. Kostrov (1974) between the tectonic stressing rate $\dot{\tau}$ and the background rate r of earthquakes, $\dot{\tau} = \langle M_0 \rangle r/V$, where $\langle M_0 \rangle$ is the mean seismic moment tensor and V the seismogenic volume of the seismicity. Assuming the same moment tensors for

all events, the scalar stressing rate can be calculated by

$$\dot{\tau} = 10^{a+9.1}\frac{b}{1.5-b}\frac{10^{(1.5-b)M_{\max}}}{AD} \quad (4)$$

for $b < 1.5$, with the surface area A, respectively, the seismogenic width D, and the Gutenberg–Richter a-value of the activity in the volume, that is, the logarithm of the $m \geq 0$ events per year (T. Dahm *et al.* 2015, eq. 1). For our estimation, a is defined by $a = \log(N_{\text{pre}}/T_{\text{pre}}) + 1.3b$ with N being the number of $m \geq 1.3$ in the polygon area A in the pre-impoundment period T, where b is set to 1.0. Furthermore, D is defined by the observed depth distribution of the seismicity and is around 10 km. The main unknown is the maximum possible magnitude $M_{\max}$. Assuming $M_{\max} \approx 7.5$ leads to a stressing rate scattering around $\dot{\tau} = 2$ kPa yr^{-1} that we used for our calculation.

Figs 7(d) and (e) show the calculated stress changes at the time of the first peak of the water level and the end of our calculation time, accounting for the tectonic stressing rate. Here, the defined mechanism with a high-angle dip of 60° is considered as the receiver mechanism, and the results for a gentle dip of 25° are presented in Fig. S8 (Supplementary Material). The plots show that the stress decreased below the lake and slightly increase northeast of it. To strengthen the analysis, we perform an additional test by calculating ΔCFS with different friction coefficients. To do this, we repeat our calculation for the effective friction coefficient ($\mu' = \mu(1-B)$) of 0.2 and 0.6. While increasing μ' from 0.2 to 0.6 slightly intensifies the negative and positive stress patterns around Lake Gotvand, the effect is insignificant (Fig. S9, Supplementary Material).

For five moderate events that occurred in the area after impoundment of the reservoir (events 46–50 in Fig. 3 and Table S5 in Supplementary Material), we estimated the stress change since the start of the impoundment accounting for the reservoir effects and the tectonic stressing rate (2 kPa yr^{-1}). We find that all of them received a positive total stress change. However, the values are low due to their far distances to the reservoir.

To estimate the seismicity changes associated with the spatiotemporal stress evolution, we first calculate the stress at a depth of 12.5 km on a spatial and temporal grid with a resolution of 0.02° and 1 d. Then, we use the Coulomb-Rate-and-State (RS) model, widely used for natural, anthropogenic and volcanic activity (J. Dieterich 1994; E.R. Heimisson & P. Segall 2018). Assuming constant normal stress, the spatiotemporal seismicity rate is given in this model by

$$R(\vec{x},t) = r(\vec{x}) \cdot \frac{K(\vec{x},t)}{1 + \frac{\dot{\tau}}{A\sigma}\int_{T_s}^{t} K(\vec{x},t')\mathrm{d}t'}$$

$$\text{with} \quad K(\vec{x},t) = \exp\left[\dot{\tau}(t-T_s) + \Delta\text{CFS}(\vec{x},t)\right]$$

where the integration starts at time T_s when the transient stress changes ΔCFS start. The background rate $r(\vec{x})$ is estimated by the smoothed seismicity calculated for the pre-impoundment period (see Fig. 7a). $A\sigma$ is the product of a constitutive parameter related to the direct effect in the laboratory-derived rate-and-state friction law and the effective normal stress acting on the faults. Since both parameters are not well constrained for natural faults, the product $A\sigma$ is taken as a free parameter, where fits of various seismic sequences yielded $A\sigma$ values between 0.01 and 0.05 MPa (S. Hainzl *et al.* 2010). The smaller $A\sigma$, the more stress changes affect the seismicity rate. Here, we set $A\sigma = 0.01$ MPa.

The result of the modelled seismicity rate in the post-impoundment period is shown in Fig. 7(f) and Fig. S8(f) (Supplementary Material), and the modelled seismicity changes with respect to the pre-impoundment period is shown in Fig. 7(g) and Fig. S8g (Supplementary Material) for selected receiver mechanisms. For the high-angle receiver faults, the modelled seismicity rate changes highlight a clear contrast between the NE and SW directions (Fig. 7g), whereas the observed seismicity rate change is more isotropic around the centre of the lake (Fig. 7c). In contrast, for the lower-angle receiver faults, the modelled seismicity rate changes are isotropic around the centre (Fig. S8g, Supplementary Material), consistent with the observations (Fig. S8c, Supplementary Material). Overall, the results based on the calculated reservoir-induced stresses are very well in agreement with the observations; in particular, the seismicity is expected to be strongly reduced in the central area of the reservoir as observed.

5 DISCUSSION

The local network (11 stations) covering the Gotvand Dam area together with IRSC and IIEES permanent seismological networks in Iran enabled us to study a 14-yr-long precise catalogue of the seismicity in this area prior to, during and after the impoundment phase, revealing clear changes due to the impoundment. The dense local network also allows focal mechanism computation of small-magnitude earthquakes. Most of the 39 focal mechanisms solutions indicate a dominant reverse mechanism, similar to the gCMT solution for moderate to large events and teleseismically computed mechanisms in this area (e.g. J. Jackson & D. McKenzie 1984; M. Talebian & J. Jackson 2004), trending NW–SE parallel to the main structures of the region (Fig. 3). These focal mechanisms and gCMT solutions for this area indicate NW-trending (300°) faults, mostly dipping towards NE with a gentle dip of 25° or a dip of 60°. The Gotvand region is one of the best examples within the Simple-Fold Belt of the Zagros, which clearly shows that the high-angle reverse faults are terminated by a very low-angle thrust fault, as mentioned by M. Berberian (1995).

By starting impoundment (2011.07.30), the temporal rate of the cumulative seismicity only slightly increased and decreased during and after impounding (Fig. 6a). Similarly, the shape of the magnitude distribution also only slightly changed with time (Fig. 4b). Furthermore, we find no evidence of any significant correlation between change of water levels and total background seismicity in the area, in contrast to other reservoirs; for example, for the Itoiz reservoir, where M.A. Santoyo *et al.* (2010) found a positive correlation between the water level variations in the lake and the occurrence of the mainshock event, or for Ataturk reservoir, where H. Eyidogan *et al.* (2010) and P. Büyükakpınar *et al.* (2021) obtained a clear anticorrelation between water level and seismicity. Thus, in the case of the Gotvand reservoir, the total seismic activity was not significantly affected by the reservoir impoundment. These findings were consistent for the events located within 20 km of the dam lake shore (Fig. S6, Supplementary Material).

However, the seismicity rates were locally strongly affected by the reservoir impoundment, as revealed by the comparison of the rate density maps prior to and after the start of the impoundment. Before impoundment, the background seismicity was concentrated in the central area of the reservoir.

There, the seismicity significantly decreased after the start of the impoundment (Figs 7a and b). This observation aligns well with the calculated time-dependent Coulomb stress changes for two dominant focal mechanisms in the area, showing significant stress shadowing below the central part of the reservoir because of the water load stabilizing thrust faulting, while stresses slightly increased in the remaining parts (Figs 7d, e and S8d, e, Supplementary Material). This observation can be attributed to the fact that seismicity triggered by reservoirs is most evident in regions with low-seismic activity and stressing rates (S. Ruiz-Barajas *et al.* 2023). Conversely, the suppression of seismicity due to water loading is more likely to be observed in highly active areas, such as the Zagros region, where a notable decrease in background activity can be detected. Despite the stress decrease below the Gotvand reservoir, seismicity modelling using the RS model only leads to reduced seismicity in the stress-shadow area instead of a shutoff. The calculated seismicity changes based on the estimated spatiotemporal stress evolution (Figs 7f, g and S8f, g, Supplementary Material) are very well in agreement with the observed seismicity patterns (Figs 7b and c). The predicted presence of seismicity in the stress shadow agrees with the observations and results from the relatively high-tectonic stressing rate. In active tectonic regions such as Zagros, the regional stress field can partly override the effects of water loading.

Induced stress due to water loading on reverse faults depends on the dip of the fault plane. Gently dipping reverse faults (dip = 25°) experience stress drops almost symmetrically beneath the lake (Fig. S8, Supplementary Material), while the stresses decrease only below and southwest of the lake for steeper faults (dip = 60°, Fig. 7). However, the estimated stress changes (drop) at seismogenic depths are smaller than 50 kPa. Thus, tectonic loading likely plays a crucial role. We estimated the tectonic scalar stressing rate to be about 2 kPa yr^{-1} in the Gotvand area. This tectonic loading contributes to the adjustment of negative stress changes in the central part of the reservoir over time. It results in a smaller area with negative Coulomb stress changes in 2019 (Figs 7e and S8e, Supplementary Material) compared to 2014 (Figs 7d and S8d, Supplementary Material). As time progresses, tectonic loading stress will dominate over the negative stress induced by impoundment in less than 25 yr.

6 CONCLUSIONS

We analysed about 14 yr of spatiotemporal seismicity recorded by a dense local network covering the Gotvand reservoir (SW Iran). Our data span the years 2006 through 2019, with impoundment started in 2011 to fill the reservoir (4.5×10^9 m^3). Calculated focal mechanisms for small earthquakes show an NW–SE-oriented reverse mechanism that agrees with the gCMT solutions for moderate and larger events and is compatible with the general trend of the existing tectonic regime in the Zagros mountain range.

To remove local aftershock activity unrelated to aseismic processes, such as tectonic forcing or reservoir-induced stresses, we used the ETAS model, recently extended to 3-D. We find that the cumulative activity in the region did not change significantly with the onset of the reservoir impoundment, neither concerning the seismicity level (rates) nor the frequency–magnitude distribution (*b*-value). However, the impoundment of Gotvand lake has significantly altered the spatial seismicity pattern, showing a notable reduction in seismic activity in the central area of the reservoir, which is in agreement with negative calculated time-dependent Coulomb stress changes for the two dominant focal mechanisms in the same area. This central part, which was highly active before the impoundment, shows a clear stress shadowing effect. Accounting for the continuous tectonic stressing in this seismically active region, the modelled seismicity evolution, based on the spatiotemporal stress changes after impoundment, can explain the observed seismicity.

ACKNOWLEDGMENTS

The authors thank the two anonymous referees for their constructive reviews that helped to improve the article. We acknowledge the International Institute of Earthquake Engineering and Seismology (IIEES), Iran Water and Power Resource Development Co. (IWPCO) and Khuzestan Water and Power Authority (KWPA) for providing the earthquake sequence data. This work has been partially funded by the Deutsche Forschungsgemeinschaft (DFG)- Project-ID 318763901—SFB1294, project B04.

AUTHOR CONTRIBUTIONS

BMA, SH and MT were involved in the general conceptualization of the study. Specifically, the ideas and research goals of this manuscript were formulated by BMA and SH. Relocation of earthquakes, preparation of the catalogue, calculation of the 1-D velocity model and focal mechanism solutions were done by MT and SSM. BMA and SH wrote the codes and performed the statistical and stress analysis. BMA wrote the original draft with major contributions of SH within all sections and MT within the second section. GZ provided the methodological overview for statistical analysis. All co-authors provided substantial feedback to the draft through their reviews.

SUPPORTING INFORMATION

Supplementary data are available at *GJIRAS* online.

suppl_data

Please note: Oxford University Press is not responsible for the content or functionality of any supporting materials supplied by the authors. Any queries (other than missing material) should be directed to the corresponding author for the paper.

DATA AVAILABILITY

The Global Centroid Moment Tensor (gCMT) focal mechanisms were downloaded from the Harvard CMT catalogue (https://www.globalcmt.org/CMTsearch.html), and the earthquake catalogue for events with magnitudes greater than 5.0 ($M > 5.0$) in the Iranian Plateau was downloaded from the USGS database (https://earthquake.usgs.gov/earthquakes/search/). The codes to reproduce the results presented in this manuscript are openly available at https://github.com/bmasayesh/Reservoir_Induced_Stress for the semi-analytical stress calculations, and on Zenodo at https://doi.org/10.5281/zenodo.14222612 (B.M.

Asayesh 2024) for parameter estimation using 3-D ETAS approaches.

REFERENCES

Alavi, M., 1980. Tectonostratigraphic evolution of the Zagrosides of Iran, *Geology,* **8**(3), 144–149.

Alavi, M., 2007. Structures of the Zagros fold-thrust belt in Iran, *Am. J. Sci.,* **307**(9), 1064–1095.

Ambraseys, N.N. & Melville, C.P., 2005. *A history of Persian earthquakes,* Cambridge University Press.

Asayesh, B.M., 2024. bmasayesh/HYBRID_ETAS: HYBRID_ETAS (Hybrid_ETAS.V.1)[Software], Zenodo.

Asayesh, B.M., Zafarani, H. & Najafi, N., 2018. Role of transferred static stress due to Sarpol-e Zahab earthquake in aftershock distribution, *J. Seismol. Earthquake Eng.,* **20**(2), 37–44.

Asayesh, B.M., Hainzl, S. & Zöller, G., 2023a. Depth-dependent aftershock trigger potential revealed by 3D-ETAS modeling, *J. Geophys. Res.: Solid Earth,* **128**(6), e2023JB026377. doi:10.1029/2023JB026377.

Asayesh, B.M., Zafarani, H., Hainzl, S. & Sharma, S., 2023b. Effects of large aftershocks on spatial aftershock forecasts during the 2017–2019 western Iran sequence, *Geophys. J. Int.,* **232**(1), 147–161.

Asayesh, B.M., Hainzl, S. & Zöller, G., 2025. Improved aftershock forecasts using mainshock information in the framework of the ETAS model, *J. Geophys. Res.: Solid Earth,* **130**(2), e2024JB030287. doi:10.1029/2024JB030287.

Awad, M. & Mizoue, M., 1995. Earthquake activity in the Aswan region, Egypt, *Pure Appl. Geophys.,* **145,** 69–86.

Bahroudi, A. & Koyi, H., 2003. Effect of spatial distribution of Hormuz salt on deformation style in the Zagros fold and thrust belt: an analogue modelling approach, *J. Geol. Soc.,* **160**(5), 719–733.

Bahroudi, A. & Koyi, H.A., 2004. Tectono-sedimentary framework of the Gachsaran Formation in the Zagros foreland basin, *Mar. Petrol. Geol.,* **21**(10), 1295–1310.

Baiesi, M. & Paczuski, M., 2004. Scale-free networks of earthquakes and aftershocks, *Phys. Rev. E,* **69**(6), 066 106. doi:10.1103/PhysRevE.69.066106.

Baiesi, M. & Paczuski, M., 2005. Complex networks of earthquakes and aftershocks, *Nonlinear Process. Geophys.,* **12**(1), 1–11.

Baker, C., Jackson, J. & Priestley, K., 1993. Earthquakes on the Kazerun Line in the Zagros Mountains of Iran: strike-slip faulting within a fold-and-thrust belt, *Geophys. J. Int.,* **115**(1), 41–61.

Barnhart, W.D., Lohman, R.B. & Mellors, R.J., 2013. Active accommodation of plate convergence in Southern Iran: earthquake locations, triggered aseismic slip, and regional strain rates, *J. Geophys. Res.: Solid Earth,* **118**(10), 5699–5711.

Berberian, M., 1995. Master "blind" thrust faults hidden under the Zagros folds: active basement tectonics and surface morphotectonics, *Tectonophysics,* **241**(3–4), 193–224.

Berberian, M. & King, G., 1981. Towards a paleogeography and tectonic evolution of Iran, *Can. J. Earth Sci.,* **18**(2), 210–265.

Büyükakpınar, P., Cesca, S., Hainzl, S., Jamalreyhani, M., Heimann, S. & Dahm, T., 2021. Reservoir-triggered earthquakes around the Atatürk Dam (southeastern Turkey), *Front. Earth Sci.,* **9,** 663 385.

Carder, D.S., 1945. Seismic investigations in the Boulder Dam area, 1940–1944, and the influence of reservoir loading on local earthquake activity, *Bull. Seism. Soc. Am.,* **35**(4), 175–192.

Chen, Y., 2009. Did the reservoir impoundment trigger the Wenchuan earthquake?, *Sci. China Earth Sci.,* **52**(4), 431. doi:10.1007/s11430-009-0067-2.

Dahm, T. *et al.*, 2010. How to discriminate induced, triggered and natural seismicity, *Proceedings of the Workshop Induced seismicity: November 15-17, 2010, Hotel Hilton, Luxembourg; Grand-Duchy of Luxembourg,* pp. 69–76, Centre Européen de Géodynamique et de Séismologie.

Dahm, T. *et al.*, 2013. Recommendation for the discrimination of human-related and natural seismicity, *J. Seismol.,* **17,** 197–202.

Dahm, T., Cesca, S., Hainzl, S., Braun, T. & Krüger, F., 2015. Discrimination between induced, triggered, and natural earthquakes close to hydrocarbon reservoirs: a probabilistic approach based on the modeling of depletion-induced stress changes and seismological source parameters, *J. Geophys. Res.: Solid Earth,* **120**(4), 2491–2509.

Davies, R., Foulger, G., Bindley, A. & Styles, P., 2013. Induced seismicity and hydraulic fracturing for the recovery of hydrocarbons, *Mar. Petrol. Geol.,* **45,** 171–185.

Deng, K., Zhou, S., Wang, R., Robinson, R., Zhao, C. & Cheng, W., 2010. Evidence that the 2008 M_w 7.9 Wenchuan earthquake could not have been induced by the Zipingpu Reservoir, *Bull. Seism. Soc. Am.,* **100**(5B), 2805–2814.

Dieterich, J., 1994. A constitutive law for rate of earthquake production and its application to earthquake clustering, *J. Geophys. Res.: Solid Earth,* **99**(B2), 2601–2618.

Ebrahimi, M., Tatar, M., Aoudia, A. & Guidarelli, M., 2018. Loading effects beneath the Gotvand-e Olya Reservoir (south-west of Iran) deduced from ambient noise tomography, *Geophys. J. Int.,* **212**(1), 229–243.

Ebrahimian, H., Jalayer, F., Maleki Asayesh, B., Hainzl, S. & Zafarani, H., 2022. Improvements to seismicity forecasting based on a Bayesian spatio-temporal ETAS model, *Sci. Rep.,* **12**(1), 20 970. doi:10.1038/s41598-022-24080-1.

Edey, A., Allen, M. & Nilfouroushan, F., 2020. Kinematic variation within the Fars Arc, eastern Zagros, and the development of fold-and-thrust belt curvature, *Tectonics,* **39**(8), e2019TC005941. doi:10.1029/2019TC005941.

Ellsworth, W.L., 2013. Injection-induced earthquakes, *Science,* **341**(6142), 1225 942.

Eyidogan, H., Geçgel, V. & Pabuçcu, Z., 2010. Correlation between water level decrease in Atatürk Dam, Turkey and M_w 5.0 earthquake on September 3, 2008, *Proc. ESC,* pp. 6–10.

Foulger, G.R., Wilson, M.P., Gluyas, J.G., Julian, B.R. & Davies, R.J., 2018. Global review of human-induced earthquakes, *Earth-Sci. Rev.,* **178,** 438–514..

Foulger, G.R., Wilkinson, M.W., Wilson, M.P. & Gluyas, J.G., 2022. Human-Induced Earthquakes: The Performance of Questionnaire Schemes, *Bull. Seism. Soc. Am.,* **112**(6), 2773–2794.

Gahalaut, K. & Hassoup, A., 2012. Role of fluids in the earthquake occurrence around Aswan reservoir, Egypt, *J. Geophys. Res.: Solid Earth,* **117**(B2). doi:10.1029/2011JB008796.

Ge, S., Liu, M., Lu, N., Godt, J.W. & Luo, G., 2009. Did the Zipingpu Reservoir trigger the 2008 Wenchuan earthquake?, *Geophys. Res. Lett.,* **36**(20). doi:10.1029/2009GL040349.

Grigoli, F. *et al.*, 2017. Current challenges in monitoring, discrimination, and management of induced seismicity related to underground industrial activities: a European perspective, *Rev. Geophys.,* **55**(2), 310–340.

Gupta, H.K., 2002. A review of recent studies of triggered earthquakes by artificial water reservoirs with special emphasis on earthquakes in Koyna, India, *Earth Sci. Rev.,* **58**(3–4), 279–310.

Gupta, H.K., Rastogi, B. & Narain, H., 1972a. Common features of the reservoir-associated seismic activities, *Bull. Seism. Soc. Am.,* **62**(2), 481–492.

Gupta, H.K., Rastogi, B. & Narain, H., 1972b. Some discriminatory characteristics of earthquakes near the Kariba, Kremasta, and Koyna artificial lakes, *Bull. Seism. Soc. Am.,* **62**(2), 493–507.

Hainzl, S., Steacy, D. & Marsan, S., 2010. *Seismicity Models Based on Coulomb Stress Calculations,* Community Online Resource for Statistical Seismicity Analysis.

Hainzl, S., Aggarwal, S., Khan, P. & Rastogi, B., 2014. Monsoon-induced earthquake activity in Talala, Gujarat, India, *Geophys. J. Int.,* **200**(1), 627–637.

Heimisson, E.R. & Segall, P., 2018. Constitutive law for earthquake production based on rate-and-state friction: Dieterich 1994 revisited, *J. Geophys. Res.: Solid Earth,* **123**(5), 4141–4156.

Hessami, K., Koyi, H.A., Talbot, C.J., Tabasi, H. & Shabanian, E., 2001. Progressive unconformities within an evolving foreland fold–thrust belt, Zagros Mountains, *J. Geol. Soc.,* **158**(6), 969–981.

Imoto, M., 2001. Point process modelling of reservoir-induced seismicity, *J. Appl. Probab.,* **38**(A), 232–242.
Jackson, J. & McKenzie, D., 1984. Active tectonics of the Alpine—Himalayan Belt between western Turkey and Pakistan, *Geophys. J. Int.,* **77**(1), 185–264.
Jamalreyhani, M. *et al.*, 2021. The 2019–2020 Khalili (Iran) Earthquake Sequence—anthropogenic seismicity in the Zagros Simply Folded Belt?, *J. Geophys. Res.: Solid Earth,* **126**(12), e2021JB022797. doi:10.1029/2021JB022797.
Keith, C., Simpson, D. & Soboleva, O., 1982. Induced seismicity and style of deformation at Nurek Reservoir, Tadjik SSR, *J. Geophys. Res.: Solid Earth,* **87**(B6), 4609–4624.
Kerr, R.A. & Stone, R., 2009. A human trigger for the great quake of Sichuan?, *Science,* **323**(5912), 322–322.
Khorrami, F. *et al.*, 2019. An up-to-date crustal deformation map of Iran using integrated campaign-mode and permanent GPS velocities, *Geophys. J. Int.,* **217**(2), 832–843.
Kissling, E., 1988. Geotomography with local earthquake data, *Rev. Geophys.,* **26**(4), 659–698.
Kostrov, B., 1974. Seismic moment and energy of earthquakes, and seismic flow of rock, *Izv. Acad. Sci. USSR Phys. Solid Earth,* **1,** 23–40.
Lei, X., 2011. Possible roles of the Zipingpu Reservoir in triggering the 2008 Wenchuan earthquake, *J. Asian Earth Sci.,* **40**(4), 844–854.
Lei, X., Ma, S.l., Wen, X., Su, J.r. & Du, F., 2008. Integrated analysis of stress and regional seismicity by surface loading—a case study of Zipingpu reservoir, *Seismol. Geol.,* **30**(4), 1046–1064.
Leith, W., Simpson, D.W. & Alvarez, W., 1981. Structure and permeability: geologic controls on induced seismicity at Nurek reservoir, Tadjikistan, USSR, *Geology,* **9**(10), 440–444.
McGarr, A., Simpson, D., Seeber, L. & Lee, W., 2002. Case histories of induced and triggered seismicity, *Int. Geophys. Ser.,* **81**(A), 647–664.
Metz, M., Maleki Asayesh, B., Mohseni Aref, M., Jamalreyhani, M., Buyukakpinar, P. & Dahm, T., 2023. July-December 2022 earthquake sequence in the southeastern Fars Arc of Zagros mountains, Iran, *Seismica,* **2**(2). doi:10.26443/seismica.v2i2.953.
Ni, J. & Barazangi, M., 1986. Seismotectonics of the Zagros continental collision zone and a comparison with the Himalayas, *J. Geophys. Res.: Solid Earth,* **91**(B8), 8205–8218.
Ogata, Y., 1998. Space-time point-process models for earthquake occurrences, *Ann. Inst. Stat. Math.,* **50,** 379–402.
Ogata, Y. & Katsura, K., 1993. Analysis of temporal and spatial heterogeneity of magnitude frequency distribution inferred from earthquake catalogues, *Geophys. J. Int.,* **113**(3), 727–738.
Oveisi, B., Lavé, J., Van Der Beek, P., Carcaillet, J., Benedetti, L. & Aubourg, C., 2009. Thick-and thin-skinned deformation rates in the central Zagros simple folded zone (Iran) indicated by displacement of geomorphic surfaces, *Geophys. J. Int.,* **176**(2), 627–654.
Pavlou, K., 2019. Relationship between observed seismicity and water level fluctuations in Polyphyto dam area (North Greece), *Memory,* **7**(16), 6. doi:10.9734/JGEESI/2019/v21i230122.
Qiu, X. & Fenton, C., 2015. Factors controlling the occurrence of reservoir-induced seismicity. *Engineering Geology for Society and Territory: Applied Geology for Major Engineering Projects, Vol. 6,* pp. 567–570, Springer.
Regard, V., Bellier, O., Thomas, J.C., Abbassi, M., Mercier, J., Shabanian, E., Feghhi, K. & Soleymani, S., 2004. Accommodation of Arabia-Eurasia convergence in the Zagros-Makran transfer zone, SE Iran: a transition between collision and subduction through a young deforming system, *Tectonics,* **23**(4). doi:10.1029/2003TC001599.
Rinaldi, A.P., Improta, L., Hainzl, S., Catalli, F., Urpi, L. & Wiemer, S., 2020. Combined approach of poroelastic and earthquake nucleation applied to the reservoir-induced seismic activity in the Val d'Agri area, Italy, *J. Rock Mech. Geotech. Eng.,* **12**(4), 802–810.
Roeloffs, E.A., 1988. Fault stability changes induced beneath a reservoir with cyclic variations in water level, *J. Geophys. Res.: Solid Earth,* **93**(B3), 2107–2124.
Ruiz-Barajas, S., Santoyo, M.Á., Benito-Oterino, M.B., Alvarado-Induni, G.E. & Climent-Martín, A., 2023. Surface water load and earthquake stress interactions near the Pirrís reservoir, Costa Rica, *Acta Geophys.,* **71,** 1–16.
Santoyo, M.A., García-Jerez, A. & Luzón, F., 2010. A subsurface stress analysis and its possible relation with seismicity near the Itoiz Reservoir, Navarra, Northern Spain, *Tectonophysics,* **482**(1–4), 205–215.
Scholz, C.H., 1990. *The Mechanics of Earthquakes and Faulting,* Cambridge University Press.
Şengör, A.C., 1984. The Cimmeride orogenic system and the tectonics of Eurasia, *Geol. Soc. Am. Spec. Paper,* **195,** 82. doi:10.1130/SPE195-p1.
Shapiro, S.A., Huenges, E. & Borm, G., 1997. Estimating the crust permeability from fluid-injection-induced seismic emission at the KTB site, *Geophys. J. Int.,* **131**(2), F15–F18.
Simpson, D.W. & Negmatullaev, S.K., 1981. Induced seismicity at Nurek reservoir, Tadjikistan, USSR, *Bull. Seism. Soc. Am.,* **71**(5), 1561–1586.
Stoecklin, J., 1968. Structural history and tectonics of Iran: a review, *AAPG Bull.,* **52**(7), 1229–1258.
Talebian, M. & Jackson, J., 2004. A reappraisal of earthquake focal mechanisms and active shortening in the Zagros mountains of Iran, *Geophys. J. Int.,* **156**(3), 506–526.
Talwani, P., 1995. Speculation on the causes of continuing seismicity near Koyna reservoir, India, *Pure Appl. Geophys.,* **145,** 167–174.
Talwani, P. & Acree, S., 1984. Pore pressure diffusion and the mechanism of reservoir-induced seismicity, *Pure Appl. Geophys.,* **122**(6), 947–965.
Tatar, M., 2010. Microseismicity of the Gotvand-e Olya Dam area based on the locally recorded earthquakes, *Annual report, IIEES*.
Tatar, M., Hatzfeld, D. & Ghafory-Ashtiany, M., 2004. Tectonics of the Central Zagros (Iran) deduced from microearthquake seismicity, *Geophys. J. Int.,* **156**(2), 255–266.
Tatar, M., Hatzfeld, D., Moradi, A. & Paul, A., 2005. The 2003 December 26 Bam earthquake (Iran), Mw 6.6, aftershock sequence, *Geophys. J. Int.,* **163**(1), 90–105.
Tatar, M., Ebrahimi, M. & Yamini Fard, F., 2011. Induced Seismicity in Masjed Soleyman Reservoir (Southwest of Iran), *Sci. Quart. J. Geosci.,* **20**(80), 95–102.
Utsu, T., Ogata, Y. & Mats'ura, R.S., 1995. The centenary of the Omori formula for a decay law of aftershock activity, *J. Phys. Earth,* **43**(1), 1–33.
Vernant, P. *et al.*, 2004. Present-day crustal deformation and plate kinematics in the Middle East constrained by GPS measurements in Iran and northern Oman, *Geophys. J. Int.,* **157**(1), 381–398.
Wiemer, S. & Wyss, M., 2000. Minimum magnitude of completeness in earthquake catalogs: examples from Alaska, the western United States, and Japan, *Bull. Seism. Soc. Am.,* **90**(4), 859–869.
Wilson, M., Foulger, G., Gluyas, J., Davies, R. & Julian, B., 2017. HiQuake: the human-induced earthquake database, *Seismol. Res. Lett.,* **88**(6), 1560–1565.
Wyss, M., Hasegawa, A., Wiemer, S. & Umino, N., 1999. Quantitative mapping of precursory seismic quiescence before the 1989, M 7.1 off-Sanriku earthquake, Japan, *Ann. Geophys.,* **42**(5), 851–869.
Yamini-Fard, F., Hatzfeld, D., Farahbod, A., Paul, A. & Mokhtari, M., 2007. The diffuse transition between the Zagros continental collision and the Makran oceanic subduction (Iran): microearthquake seismicity and crustal structure, *Geophys. J. Int.,* **170**(1), 182–194.
Zaliapin, I. & Ben-Zion, Y., 2013. Earthquake clusters in southern California I: Identification and stability, *J. Geophys. Res.: Solid Earth,* **118**(6), 2847–2864.
Zaliapin, I., Gabrielov, A., Keilis-Borok, V. & Wong, H., 2008. Clustering Analysis of Seismicity and Aftershock Identification, *Phys. Rev. Lett.,* **101**(1), 018 501. doi:10.1103/PhysRevLett.101.018501.